Numerical simulations of grass fires using a coupled atmosphere–fire model: Basic fire behavior and dependence on wind speed

Rodman R. Linn
Earth and Environmental Sciences Division, Los Alamos National Laboratory, Los Alamos, New Mexico, USA

Philip Cunningham
Department of Meteorology and Geophysical Fluid Dynamics Institute, Florida State University, Tallahassee, Florida, USA

Received 10 November 2004; revised 10 March 2005; accepted 8 April 2005; published 6 July 2005.

[1] Numerical simulations using a fire model, FIRETEC, coupled to an atmospheric dynamics model, HIGRAD, are examined to investigate several fundamental aspects of fire behavior in grasslands, and specifically the dependence of this behavior on the ambient atmospheric winds and on the initial length of the fire line. The FIRETEC model is based on a multi-phase transport approach, and incorporates representations of the physical processes that govern wildfires, such as combustion and radiative and convective heat exchange. Results from the coupled model show that the forward spread of the simulated fires increases with increasing ambient wind speed, and the spread rates are consistent with those observed in field experiments of grass fires; however, the forward spread also depends significantly on the initial length of the fire line, and for a given ambient wind speed the spread rate for long (100 m) lines is greater than that for short (16 m) lines. The spread of the simulated fires in the lateral direction also depends on the ambient wind speed and the length of the fire line, and a possible explanation for this effect is given. For weak ambient winds, the shape of the fire perimeter is dramatically different from that seen with higher wind speeds. The shape of the fire perimeter is also shown to depend on the initial length of the fire line. These differences in fire behavior are attributed to the differences in the nature of the coupled atmosphere–fire interactions among these cases, and are described in terms of the complex interplay between radiative and convective heat transfer.

Citation: Linn, R. R., and P. Cunningham (2005), Numerical simulations of grass fires using a coupled atmosphere–fire model: Basic fire behavior and dependence on wind speed, *J. Geophys. Res.*, *110*, D13107, doi:10.1029/2004JD005597.

1. Introduction

[2] Wildfires are highly complex geophysical phenomena involving interactions between the combustion processes, the local atmospheric environment, and the terrain and vegetation characteristics. Wildfires in grasslands are a special case of considerable interest, not only because they contribute to a significant portion of wildfires worldwide, but also because, despite their relatively benign appearance in comparison to devastating high-intensity fires in timber or logging slash, they are responsible for a large proportion of firefighter fatalities and injuries [e.g., *Wilson and Sorenson*, 1978]. Fires in open fine fuels such as grass fields are highly responsive to the wind, and changes in wind speed or direction can lead to rapid changes in fire behavior that may be potentially dangerous for suppression operations. Indeed, many so-called "blowup fires" (i.e., fires that exhibit rapid increases in rate of spread and intensity) occur in deceptively light fuels [e.g., *Wilson and Sorenson*, 1978].

0148-0227/05/2004JD005597

[3] Despite their importance as a natural phenomenon, a great deal remains unknown about wildfire behavior (e.g., spread rate, intensity, flame length and height) and its coupling with the atmosphere, largely due to the difficulty involved in obtaining detailed data in fires and the surrounding environment. Laboratory experiments [e.g., *Carrier et al.*, 1991; *Wolff et al.*, 1991; *Weise*, 1993; *Catchpole et al.*, 1998] can provide comprehensive data sets and a high degree of repeatability, but the degree of relevance of these experiments to wildland fires remains to be determined, especially with respect to atmosphere–fire interactions. On the other hand, field experiments [e.g., *Sneeuwjagt and Frandsen*, 1977; *Cheney et al.*, 1993, 1998; *Cheney and Gould*, 1995] can provide information about the gross aspects of real wildland fire behavior and its dependence on the average ambient atmospheric conditions and fuel properties, but the inhomogeneous and transient nature of the atmosphere, coupled with uncertainties in the fuel characterization and the essentially unrepeatable nature of the experiments, lead to large uncertainties in the results. Nevertheless, it is worth mentioning that field experiments of grass fires [e.g., *Cheney et al.*, 1993; *Cheney and Gould*,

1995] indicate that, for continuous fuels of uniform moisture content, the rate of forward fire spread depends primarily on the wind speed and the width of the head fire (i.e., the length of the fire line perpendicular to the direction of spread), while other variables such as fuel load and grass species, which also can affect spread rate, sometimes have a less significant impact. The fact that spread rate increases with wind speed is widely accepted, but the nature of the interplay between physical processes that change with wind speed and thus change fire behavior is less well understood.

[4] In recent years, coupled atmosphere–fire modeling has emerged as a viable approach to investigating aspects of wildland fire behavior. A numerical simulation approach can augment the experimental approaches in a complimentary manner, particularly when the latter are used as a reality check for the former. Nevertheless, modeling fire is a problem of immense complexity.

[5] The differences in scale between the chemical processes occurring within the fire and the atmospheric processes occurring in the fire environment typically span several orders of magnitude, and thus it is seldom feasible to simulate all the details of the coupled atmosphere–fire system over domains large enough to capture wildland fire behavior. To model fire behavior on the landscape scale (i.e., over distances of ~300 m and greater), significant approximations must be made in order to represent the combined essence of small-scale chemical and physical processes and of the fuel structure so that computations are not prohibitively expensive. As a result, the simulation of wildfires requires a different type of model from those employed in traditional high-resolution combustion modeling, which often resolve scales much smaller than centimeters but are restricted to domain sizes on the order of ten meters.

[6] Several different approaches to simulating the coupled atmosphere–fire system have been presented in the recent literature. *Clark et al.* [1996a, 1996b, 2004] coupled empirical fire spread models to a high-resolution atmospheric model and were able to describe several aspects of behavior that appear to be common to observed fires, while in a recent paper *Clark et al.* [2003] built on this basic approach by incorporating a subgrid-scale parameterization of combustion. Other investigators have adopted approaches to coupled atmosphere–fire modeling that draw heavily from traditional combustion modeling [e.g., *Grishin*, 1997; *Larini et al.*, 1998; *Porterie et al.*, 2000; *Morvan and Dupuy*, 2001; *Rehm et al.*, 2003]. These models incorporate a more complete treatment of the chemical processes inherent to combustion in wildland fuels, but in doing so are restricted to simulating fire spread over relatively small distances, and often only in two dimensions.

[7] Another approach to modeling the coupled system was developed by *Linn* [1997] and *Linn and Harlow* [1998]. This model, called FIRETEC, is entirely physics-based and therefore self-determining rather than empirical. It is coupled with an atmospheric model called HIGRAD [*Reisner et al.*, 2000], so as to describe the dynamics of wildfires in a fully three-dimensional configuration under arbitrary meteorological conditions with large variations in terrain and vegetation type and distribution [*Linn et al.*, 2002]. This approach accounts for the transport of temporally and spatially varying atmospheric species (i.e., oxygen), and includes the treatments of turbulence and chemistry necessary to account for energy production and transport (both advective and radiative) and fuel depletion, in the presence of self-determining variations of wind speed and direction (both local and mesoscale). A similar approach was also developed by *Grishin* [1997], but computational limitations restricted the scope of his studies.

[8] In previously reported studies, the HIGRAD/FIRETEC modeling system was applied to situations with large inhomogeneities of vegetation and complex, realistic terrain structure [*Linn et al.*, 2002]. In this paper, however, we return to the deceptively simple-appearing problem of fires in homogeneous fuels on flat ground in order to examine the extent to which the dynamics of the three-dimensional coupling between the atmosphere and the fire depends on wind speed. As has been found in both laboratory and field experiments, wind speed has a leading-order impact on fire behavior; however, despite this fundamental importance, many aspects of this dependence remain poorly understood [*Beer*, 1991, 1993], although early results from coupled atmosphere–fire models have shed some light on the issue [*Clark et al.*, 1996a]. Furthermore, because the field experiments by *Cheney et al.* [1993] and *Cheney and Gould* [1995] indicate a significant dependence of fire spread on the length of the fire line, we also explore the impact of fire line length on fire behavior. Although HIGRAD/FIRETEC is capable of simulating fires in complex vegetation structures, rugged topography, and evolving winds [e.g., *Linn et al.*, 2002], in this study we have chosen to simulate fires on flat ground with homogeneous fuel loads and moistures in the presence of constant ambient winds in an effort to focus on these interactions without additional complications caused by topography, inhomogeneous fuels, or variable winds. It is important to note, however, that the specification of the fuel in the model is based on the physical properties of the vegetation, and therefore can be applied to fuels of essentially arbitrary type and distribution [e.g., *Linn et al.*, 2002].

[9] The plan of the present paper is as follows. In the next section, we describe briefly the governing equations of the FIRETEC model, and outline the simulations to be presented. In section 3 we describe in detail the results of the simulations, while section 4 presents a comparison of these results with predictions from empirical models of fire spread commonly used for operational purposes (based on the equations of *Rothermel* [1972] and *Cheney et al.* [1998]). In section 5, we present the overall conclusions of the present study.

2. Model Formulation and Description of Simulations

[10] In this section, we provide an overview of the formulation of the FIRETEC model, numerical solution methods, and describe the parameters chosen for the simulations to be shown in this paper.

2.1. Formulation of the FIRETEC Model

[11] The FIRETEC model is a multi-phase transport model, based on the ensemble-averaged conservation equations for mass, momentum, energy, and chemical species. FIRETEC, which can be used for solution of two- or three-dimensional problems, couples models for macroscale effects

of processes such as combustion, radiation, convective heat exchange, and aerodynamic drag in order to achieve an entirely self-determining coupled atmosphere–fire model. The physical and chemical formulations of the FIRETEC model are described in detail by *Linn* [1997], with several modifications given by *Linn et al.* [2002]. For the present paper, the basic equations are summarized in Appendix A.

[12] Many researchers have developed high-fidelity combustion models for different applications such as jet fuel pool fires or coal combustion; however, in these applications the fuel makeup and geometry often are reasonably well known and are limited in size (usually only up to tens of meters). This type of detailed combustion modeling is more difficult in the context of wildfire modeling where the solid fuel is not resolved and is highly heterogeneous. For this reason, the complex set of chemical reactions occurring in a wildland fire are described in the FIRETEC model by a single solid–gas reaction, consisting of wood reacting with oxygen ultimately to produce inert gases and heat. The effects of hydrocarbon pyrolysis and the transport of burning gas through the atmosphere are, for the present, represented by a single local reaction. The goal of this net reaction model is to capture the combined essence of the many complex reactions that are not resolvable. Consequently, it is assumed that the rate of the net exothermic reaction is limited by the rate at which reactants are brought together in their correct proportions (i.e., the reaction is mixing limited). Although such an approach represents a simplification of the processes of combustion, it is motivated by the expectation that the dominant exothermic reactions in a fire involve the oxidation of hydrocarbons, which are produced by the pyrolysis of solid fuels: if either fuel or oxygen is absent, the complex chain of reactions is broken. In addition, if the solid fuel temperature drops below the pyrolysis temperature the combustion is also halted. Given that the smallest resolved scale in the model is on the order of a meter, and since the model does not attempt to resolve flames explicitly, it is suggested that such a simple approach is justified as a starting point for the present study of coupled atmosphere–fire behavior.

[13] With this net chemistry model, the reaction rate is formulated as a function of the relative densities of vegetation and oxygen, the turbulent diffusion coefficient, the stoichiometric coefficients, and a probability distribution function for the temperature within a finite-difference grid volume (see *Linn* [1997, pp. 77–79] for conceptual details). This probability distribution function approach is formulated based on the assumption that there are unresolved temperature fluctuations; the integral of the probability distribution function over temperatures above a critical value represents the mass fraction of a resolved volume that is hot enough to pyrolyze.

[14] The evolution of the local mass of solid fuel per unit volume of space, ρ_f (referred to as the macroscopic density of the vegetation, which is equal to the material density of the vegetation times the local volume fraction of the vegetation), is represented using a partial differential equation that accounts for the mass loss due to the chemical reactions. The depletion of the macroscopic density of liquid water associated with the vegetation is modeled using a partial differential equation that accounts for the evaporation of water, the rate of which is modeled based on the temperature and the energy balance of the solid fuel. The formulation for this evaporation rate is also based on the assumption that there will be a temperature distribution for the solid fuel within a finite-difference cell and that, even if the average temperature of the vegetation is not above the boiling point of water, there is likely to be a fraction of that solid fuel that is hot enough to begin losing water, and therefore to begin losing heat and mass. As the average temperature rises, more water is allowed to evaporate since it is assumed that a larger percentage of the mass is above the boiling point of water.

[15] The evolving temperature of the vegetation (i.e., the solid fuel), T_s, is calculated using a partial differential equation for the specific internal energy of the solid fuel per unit volume of space. This partial differential equation includes terms that model absorption and emission of thermal radiation, exchange of energy with the gases around the solid through convective heat exchange, and energy loss and production terms associated with the chemical reaction and water evaporation. The density of the combined set of gases is predicted using a transport equation that accounts for the movement of gases from one location to another and the creation of new gases through the pyrolysis process and the evaporation of water, and the momentum of the gases is predicted using a transport equation that includes advection, gravity, and pressure gradient terms. The transport equation for the momentum of the gas also includes terms that represent the effects of unresolved turbulence on the mean flow and the drag induced by the vegetation. The evolution of the density of gaseous species such as oxygen is also modeled with a transport equation that represents the advection and diffusion of species due to turbulence, as well as the depletion of the species due to chemical reactions. The transport equation for the potential temperature of the gas accounts for advection and diffusion processes as well as convective heat transfer with the solid, radiation losses from the hot gases, and the energy produced by the chemical reactions.

[16] An important aspect of the FIRETEC model is the treatment of the turbulent Reynolds stress, R_{ij}, and the turbulent kinetic energy. The turbulent kinetic energy is associated with a spectrum of length scales; in the context of wildfires we expect that there is more than one dominant length scale for which there is a high concentration of turbulent kinetic energy, and we expect that in many cases the length scales will be associated with the vegetation geometry (e.g., for grass lands these scales might be determined by the distance between clumps of grass, the height of the grass, the distance between blades, etc.). Further above the ground, the fluctuations that accompany more complex wind fields higher in the atmosphere are sufficiently large in scale to be resolved explicitly in the calculations and are not represented by the turbulence transport equations. In FIRETEC, the turbulent kinetic energy is modeled at more than one fixed length scale: turbulence is represented as the sum of three separate turbulent kinetic energy quantities corresponding to three length scales, chosen herein to be 1 m, 0.25 m, and 0.1 m. This approach then requires supplementing the governing equations for turbulence with one additional transport equation for each turbulent kinetic energy at each scale. The Reynolds stress at each scale is then represented in

Table 1. Simulation Parameters

Simulation	Ambient Wind Speed, U_{in}, m s^{-1}	Domain Size in (x, y), m	Ignition Line Length, m
U01SHORT	1.0	160 × 160	16.0
U01LONG	1.0	160 × 160	100.0
U03SHORT	3.0	160 × 160	16.0
U03LONG	3.0	160 × 160	100.0
U06SHORT	6.0	160 × 160	16.0
U06LONG	6.0	160 × 160	100.0
U12SHORT	12.0	320 × 160	16.0
U12LONG	12.0	320 × 160	100.0

terms of the Boussinesq approximation derived from the resolved velocity strain rates and the total turbulent kinetic energy associated with each length scale. A more complete description of this treatment of turbulence is provided by *Linn* [1997], and the salient features are reproduced here in Appendix B.

[17] The radiation flux to the gas is treated via a two-field thermal radiation scheme with many similarities to that described by *Stephens* [1984]. This scheme employs a three-dimensional transport approximation analogous to that for thermal heat transfer through a medium that may be optically thin.

2.2. Simulations

[18] The governing equations of the HIGRAD/FIRETEC modeling system are solved numerically via a conservative forward-in-time technique based on a method of averages (MOA) approach, in which high-frequency waves are treated explicitly in a computationally efficient manner as described by *Reisner et al.* [2000]. HIGRAD/FIRETEC can be run at a variety of resolutions, but all of the simulations described in this paper use a horizontal-direction grid spacing that is uniform and equal to 2 m, and a vertical-direction grid spacing that is nonuniform, with a grid spacing near the ground of approximately 1.5 m increasing to about 30 m at the top of the domain at z = 615 m. Because simulated fires in the presence of a weak wind do not spread as quickly as do fires in the presence of strong winds, and thus spread shorter distances for the same amount of simulated time, the horizontal dimensions of the domain are different for different simulations depending on the ambient wind speed. The domain size employed for each simulation is provided in the following section, along with the other input parameters that define the simulations.

[19] For each simulation with HIGRAD/FIRETEC, there are numerous input data that must be supplied to describe the initial state and the boundary conditions. A wide variety of choices are available for the types and locations of the fuel, the configuration of terrain, and the incoming flux of wind. As mentioned previously, the objective of the simulations is to provide a basis upon which to study the interactions of the atmospheric and fire processes that impact and control fire behavior. With this objective in mind, all simulations shown here have a fuel bed load that is specified to be similar to tall grass of height 0.7 m, with an area distribution of 0.7 kg m^{-2}, contained within the first grid cell above the ground. Thus the fuel bed is rather coarsely resolved, but other studies have shown that this resolution is sufficient to exhibit the essential characteristics and effects of the fuel for heading fires. Within the fuel bed, the surface area per unit volume of the fuel is specified as 4000 m^{-1}, which is typical for tall grass [e.g., *Rothermel*, 1972; *Burgan*, 1988]. The sensitivity of the results to the value chosen for the parameter is not obvious, however, and may not be trivial since a lower surface area per unit volume will reduce drag, thus allowing higher wind speeds near the ground, and will reduce the area through which energy can exchange between the solid and gas phases.

[20] The heat of combustion is 8914 kJ kg^{-1} of total reactants, or 19378 kJ kg^{-1} of solid fuel, which is given by *Drysdale* [1998] as a general heat of reaction for the type of circumstances described herein. This value can vary considerably for different types of vegetation based on percentages of lignin, cellulose, and hemicellulose, but we have not investigated the effects of this variation for the present circumstances. The initial fuel moisture fraction (i.e., the mass of water divided by the mass of fuel) is 0.05.

[21] Since the primary goal of the present paper is to explore the fundamental dynamics of coupled atmosphere–fire behavior and its dependence on the ambient atmospheric wind speed, simulations have been performed for several different values of the inlet wind speed, U_{in}, as indicated in Table 1. Larger domains are used for the stronger ambient wind speeds to ensure that the fire remains within the domain; the domain sizes are also given in Table 1. The ambient wind speed is taken to be in the positive x direction and is initialized with a uniform vertical profile. In the very early stages of the simulation a vertical shear profile develops near the ground due to the drag associated with the vegetation. The profile develops over the majority of the domain within seconds after the beginning of the simulations and at the inlet long before the flow reaches the ignition location (100 m in from the inlet). The ambient atmospheric stability is taken to be neutral in all cases shown here, and the Coriolis parameter is neglected.

[22] In order to examine the behavior of the fire as it spreads it is necessary to initiate the fire itself in the model. As with many of the other elements of these simulations this is performed in a simple fashion. The fire is "ignited" by removing any fuel moisture and raising the mean temperature of the fuel steadily from 300 K to 1000 K over 2 s within a rectangular area on the lowest grid level of the domain. Since we are interested in the dependence of fire behavior on the length of the fire line as well as on the ambient wind speed, we choose two different values for the initial fire line length in the cross-wind (i.e., y) direction. For the purposes of this paper, we have chosen these lengths based on analysis of previous simulations and on photographs from experimental studies such as *Cheney et al.* [1993] and *Cheney and Gould* [1995]. We consider line lengths of 16 m, which will be referred to as the "short line", and 100 m, which will be referred to as the "long line". In all cases, the width of the ignition line is 4 m in the x-direction, and the line is located at 100 m from the inlet boundary. The ignition line length for each simulation is provided in Table 1.

3. Results

[23] For the purposes of the present paper, the downwind propagation distance of the fire front is associated with the farthest downwind location where the temperature of the solid fuel is raised to 500 K. The spread rate is taken to be

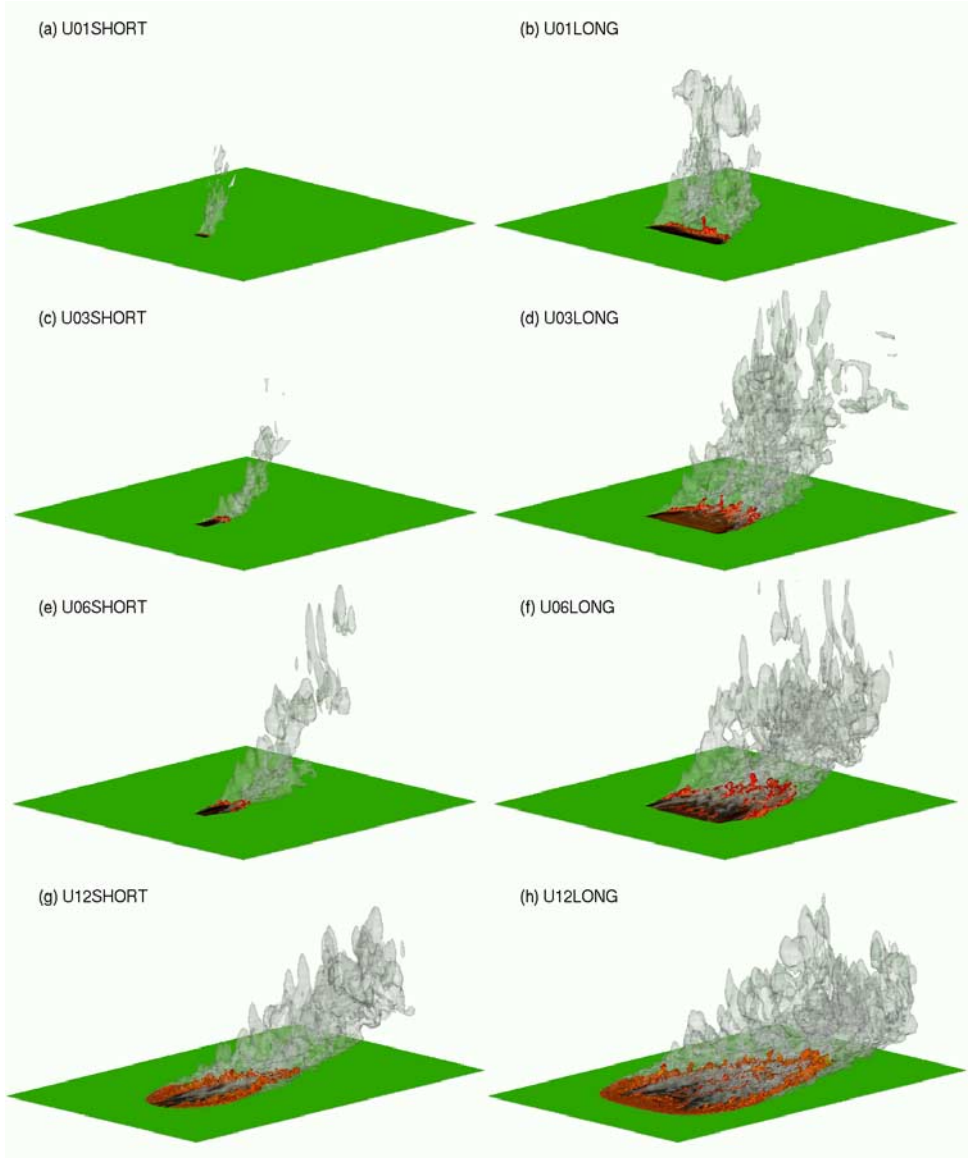

Figure 1. Isosurfaces of potential temperature (orange) and oxygen concentration (0.2, gray; 0.05, red) at t = 100 s for (a) U01SHORT, (b) U01LONG, (c) U03SHORT, (d) U03LONG, (e) U06SHORT, (f) U06LONG, (g) U12SHORT, and (h) U12LONG. The horizontal surface depicts solid fuel depletion (green indicates zero depletion, black indicates depletion).

the time derivative of this propagation distance. As will be discussed further below, these quantitative results have provided plausible speculative explanations for some of the fire behavior demonstrated by the simulations.

[24] Three-dimensional depictions of all eight simulations at 100 s after ignition are displayed in Figure 1, which shows three-dimensional isosurfaces of potential temperature, θ, and oxygen concentration, ρ_o/ρ_g, as well as contours of solid fuel depletion at the bottom grid cell. This figure shows that the farther the fire front has progressed at the depicted moment, the greater is the spread rate in that case. It is then apparent that the forward and lateral spread rates increase with increasing ambient wind speed. This is true both for the short-line cases (Figures 1a, 1c, 1e, and 1g) and for the long-line cases (Figures 1b, 1d, 1f, and 1h). It is also evident that for a given ambient wind speed, the spread rate of the head fire is greater for the long line than for the short line (compare Figure 1a with Figure 1b, Figure 1c with Figure 1d, Figure 1e with Figure 1f, and Figure 1g with Figure 1h). This behavior is consistent with the field experiments described by *Cheney et al.* [1993] and *Cheney and Gould* [1995], although it should be noted that in the simulations this effect is slightly greater for low wind speeds than for high wind speeds, whereas the experiments reported in *Cheney and Gould* [1995] indicate that this effect is greatest at high wind speeds.

[25] The plume associated with the fire in each simulation is depicted in Figure 1 by the 0.2 isosurface of oxygen concentration; these isosurfaces correspond closely to potential temperature isosurfaces, and as such provide a qualitative measure of both the integrated mass loss rate and the heat production rate associated with the fire. As the ambient wind speed increases, the plume increases in size and with increasing fire line depth (i.e., the horizontal extent

of the actively burning region in the along-wind direction). The plumes are also larger for the long-line fires than for the short-line fires, which is to be expected given the larger burning area in the long line cases. It is also observed that the downwind tilt of the plume depends on the ambient wind speed; in this regard, the plume is clearly more tilted for stronger ambient winds.

[26] Figures 2–5 show the progression of the fire perimeter and the wind velocity vectors for all the simulations. The wind velocity vectors are shown at z = 2.26 m – located 1.56 m above the fuel bed – for the time corresponding to the outer (i.e., latest) perimeter. This height is chosen because it corresponds to the height of the center of the first computational cell that is completely above the vegetation.

[27] It is evident from these figures that not only does the spread rate depend on the ambient wind speed and the line length, but so also does the structure and evolution of the fire itself. The shape and lateral spread of the fire differ substantially from case to case; however, it does appear that as the ambient wind speed increases, the shapes of the fire perimeters become more similar to each other (i.e., the shape becomes less sensitive to incremental wind speed changes at higher wind speeds). In these cases, the fire shape resembles the double ellipse, or ovoid shape that is commonly observed in wind-driven fires [e.g., *Fons*, 1946; *Anderson*, 1983]. As an example in this regard, the evolution of the fire perimeter seen in the U01LONG case (Figure 2b) is considerably different from that seen in the U03LONG case (Figure 3b), whereas the perimeters in the U06LONG (Figure 4b) and U12LONG (Figure 5b) cases are quite similar. This difference in behavior appears to be a consequence of a change in the nature of the atmosphere–fire interactions as the ambient wind speed increases.

[28] The vectors in Figures 2–5 display some consistent patterns related to the influence of the fire on the wind field at a height of 1.56 m above the fuel bed. The most significant components of the wind field in the y-direction at this height occur slightly ahead (downstream) of the fire front, whereas the most significant components of the wind field in the x-direction are located inside the burned out area immediately behind the fire front (where there is less drag and where the indraft of the fire is complementing and enhancing the ambient wind). These features of the simulations are consistent with field observations of fires, which indicate that the wind increases over the burnt area and is strongest just behind the combustion zone.

[29] The interaction between the atmosphere and the fire can be understood in terms of the physical processes that control the spread of the fire by heating fuel outside the fire line in order to drive off the moisture and cause it to begin to burn actively. For this purpose we consider the roles of the radiation heat transfer, the convective heat transfer associated with mean (i.e., resolved) winds driven by the buoyant forces and by the ambient wind, and the movement of hot gases by turbulent fluctuations. Heat can be transferred from the intensely burning regions to nearby cooler and unburned fuel by radiation heat transfer and turbulent gusts of hot air, which heat the unburned fuel through convective heat exchange. Simultaneously, there are mean-flow air currents that carry heat from one place to another. Depending on the direction of these mean-flow air currents, they can transfer energy from hot regions to cooler regions or they can transfer energy from areas that are only slightly warmer than ambient into burning regions. Consideration of the trends of these heat transfer processes as a function of wind speed and line length allows for an assessment of how the spread of the fire in various directions depends on local and nonlocal characteristics of the fire and the environment. A detailed quantitative description of these processes is critical and will be the focus of future work.

[30] As the ambient wind speed increases, the thermal radiation from burning regions to unburned fuel in front of the head fire may increase both because the depth of the fire line in the direction of the wind and the fire intensity tend to increase and thus the amount of burning material increases, and because the radiation view factor from hot gases and soot to the unburned fuel downwind of the fire increases as the plume angle decreases. The convective heat transfer due to the mean flow also increases with wind speed since stronger winds are able to penetrate through the plume more effectively, and thus are able to transfer more heat towards the unburned fuel than are weaker winds. At lower wind speeds, the flow near the ground may be dominated by the indrafts at the base of the plume, and in some cases the wind ahead of the fire may be redirected completely, drawing cool air over the unburned fuel resulting in convective cooling in this region, potentially reducing the forward rate of spread. In this regard, the flows induced by the fire (i.e., buoyant plumes and their associated vorticity patterns) have a greater effect on the transport of hot gases towards or away from unburned fuel in the presence of weak ambient winds than they do in the presence of strong winds. The transfer of heat from the burning region to unburned fuel via turbulent mixing is diffusive in nature and thus will be associated with heat transfer from hot areas to cooler areas; however, the strength of this process will depend significantly on the strength of the shear and the amount of heat being produced by the fire. With increasing wind speeds and the associated increases in fire line depth, there will be increases in the strength of the turbulence due to increases in wind shear and buoyancy induced perturbations, the net effect of which will be to increase the turbulent transport of heat from burning regions to unburned regions.

[31] These heat transfer processes also will depend on the length of the fire line, although in this regard it should be noted that there are several contributions to this dependence, some of which themselves will depend upon wind speed. These contributions include the radiation heat transfer to the unburned fuel in front of the fire, which would be expected to increase as the fire line length increases due to the enhanced thermal contributions associated with this increased length. Such an effect is likely to be most significant in the context of weak ambient wind speeds, since the importance of radiation is increased in this case. It is also likely that the convective heat transfer by the mean flow will increase with line length, since the wind has less ability to blow around the fire and therefore must penetrate through the fire line, carrying hot gases towards the unburned fuel in front of the fire. These heat transfer processes are discussed in further detail below in conjunction with more detailed descriptions of the simulated fire behavior in each case. With respect to the forward spread of

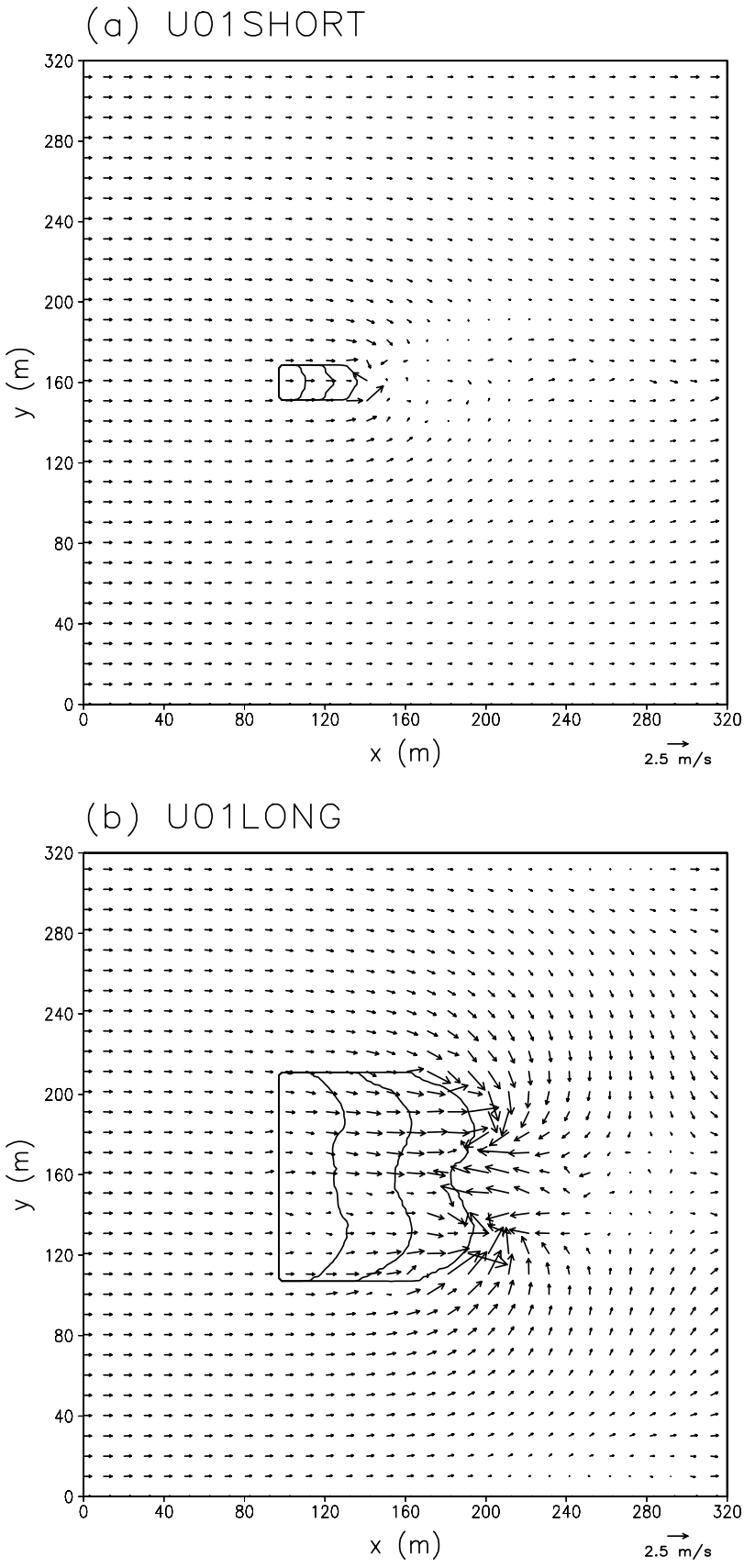

Figure 2. Plan view of the fire perimeter at t = 120 s, 240 s, and 360 s for the simulations with ambient winds of 1 m s^{-1}: (a) U01SHORT and (b) U01LONG. Also shown are horizontal wind vectors at z = 2.26 m for t = 360 s (vectors plotted every 10 m).

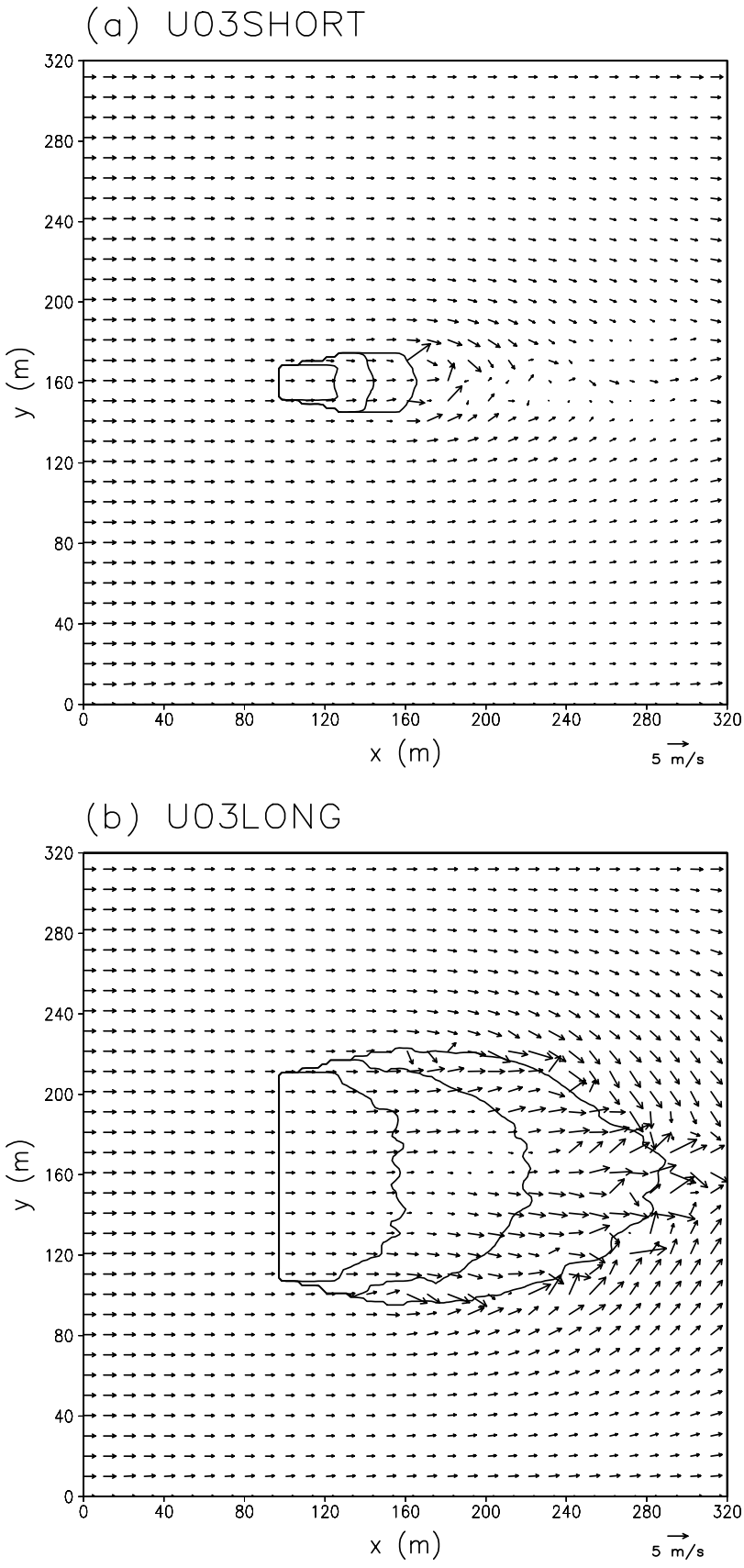

Figure 3. Plan view of the fire perimeter at t = 80 s, 160 s, and 240 s for the simulations with ambient winds of 3 m s^{-1}: (a) U03SHORT and (b) U03LONG. Also shown are horizontal wind vectors at z = 2.26 m for t = 240 s (vectors plotted every 10 m).

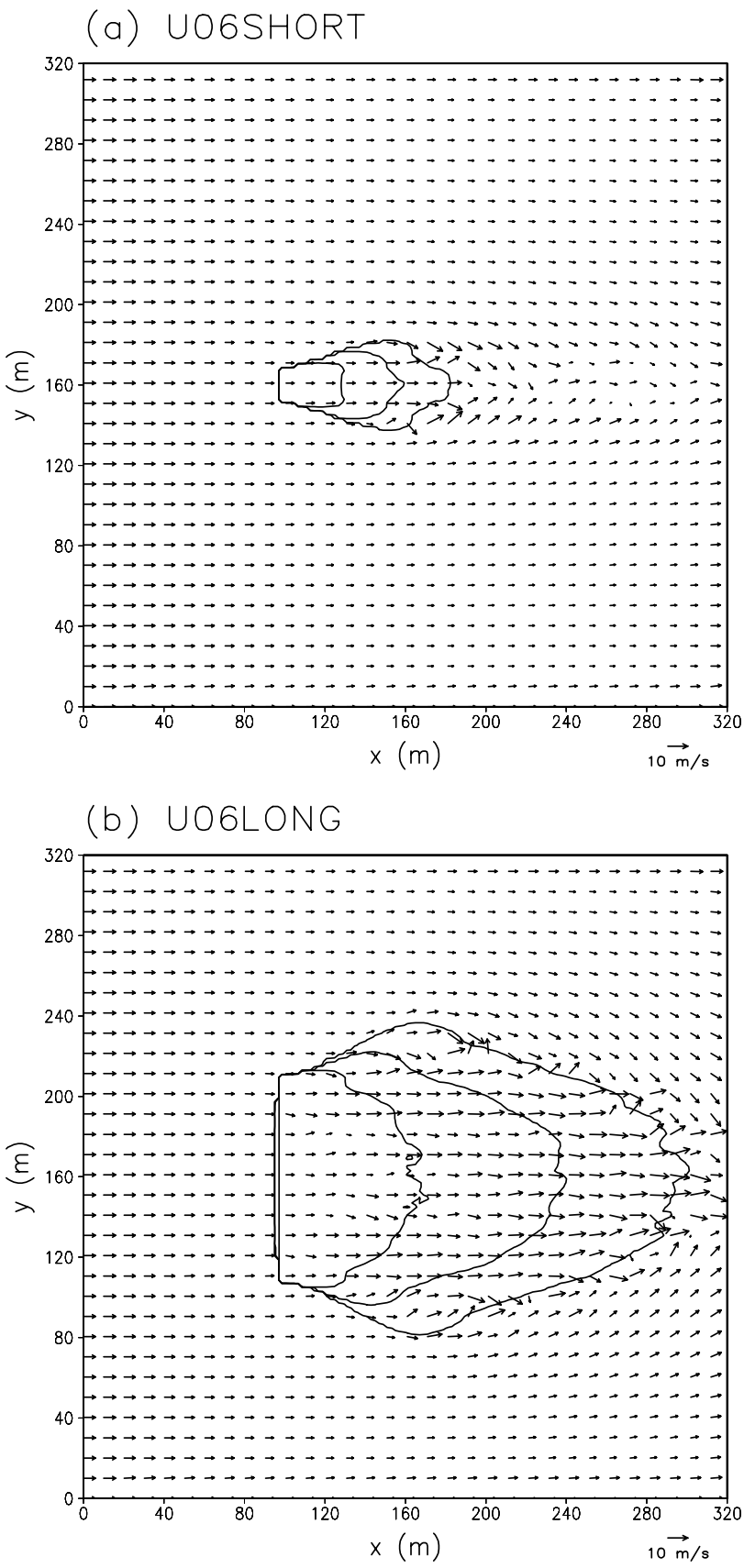

Figure 4. Plan view of the fire perimeter at t = 50 s, 100 s, and 150 s for the simulations with ambient winds of 6 m s^{-1}: (a) U06SHORT and (b) U06LONG. Also shown are horizontal wind vectors at z = 2.26 m for t = 150 s (vectors plotted every 10 m).

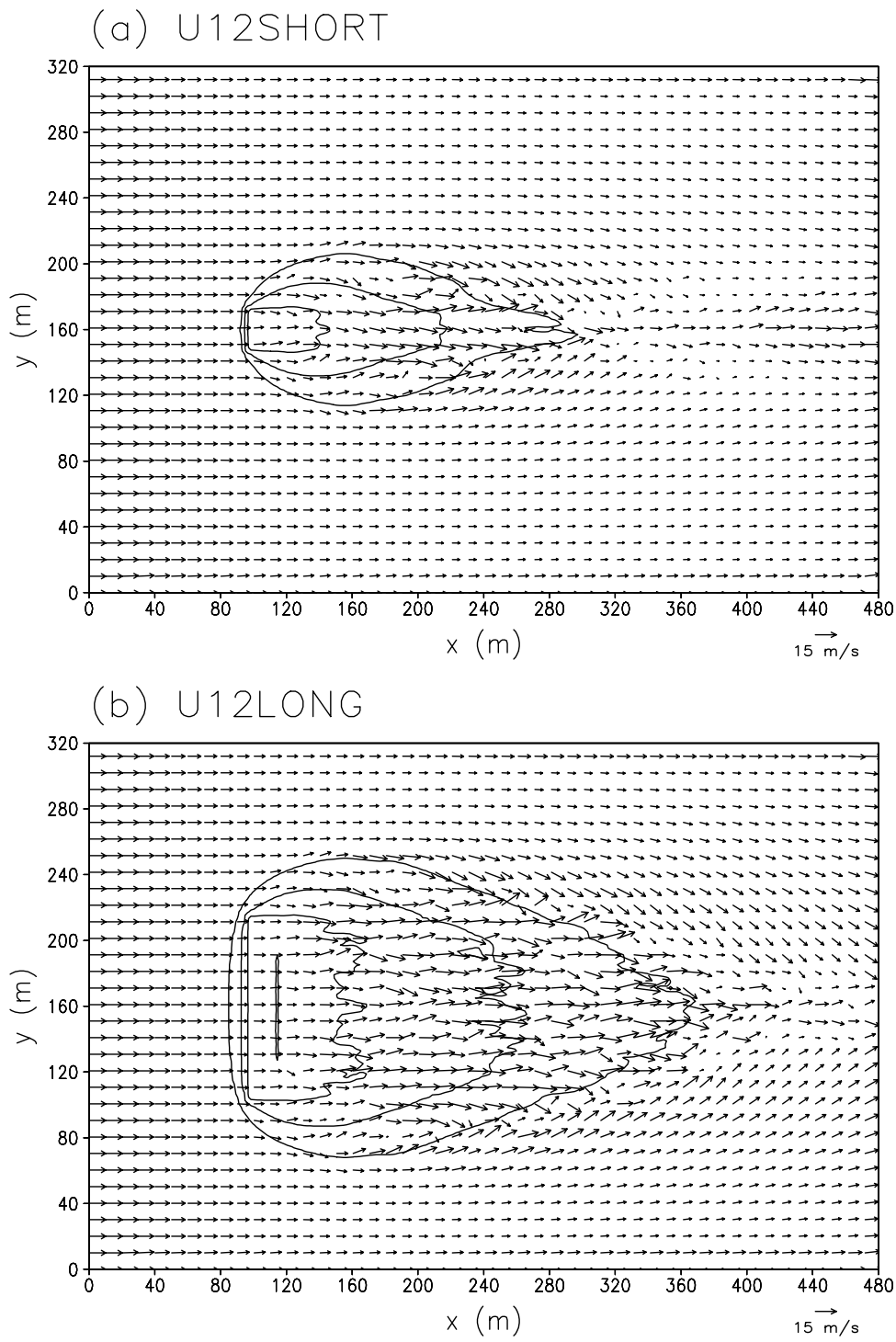

Figure 5. Plan view of the fire perimeter at t = 30 s, 60 s, and 90 s for the simulations with ambient winds of 12 m s^{-1}: (a) U12SHORT and (b) U12LONG. Also shown are horizontal wind vectors at z = 2.26 m for t = 90 s (vectors plotted every 10 m).

the head fire (i.e., the portion of the fire line that is spreading in the direction of the ambient wind), it should be noted that all of these heat transfer processes work together to spread the fire, except in the case of weak winds as noted above, where the low-level entrainment into the fire may result in convective cooling at the head fire.

[32] It is also of particular interest to examine the spread of the lateral fire line (i.e., the portion of the fire line that moves in the crosswind direction, often called the "flanking fire line") in the context of these heat transfer mechanisms. In this regard, a schematic representation of the combined processes that transfer heat to unburned fuel is shown in Figure 6 for two different types of fire lines. In both panels, three vectors representative of heat transfer are shown: net radiation heat transfer from the intensely burning region to the unburned fuel, convective heat transfer to the unburned

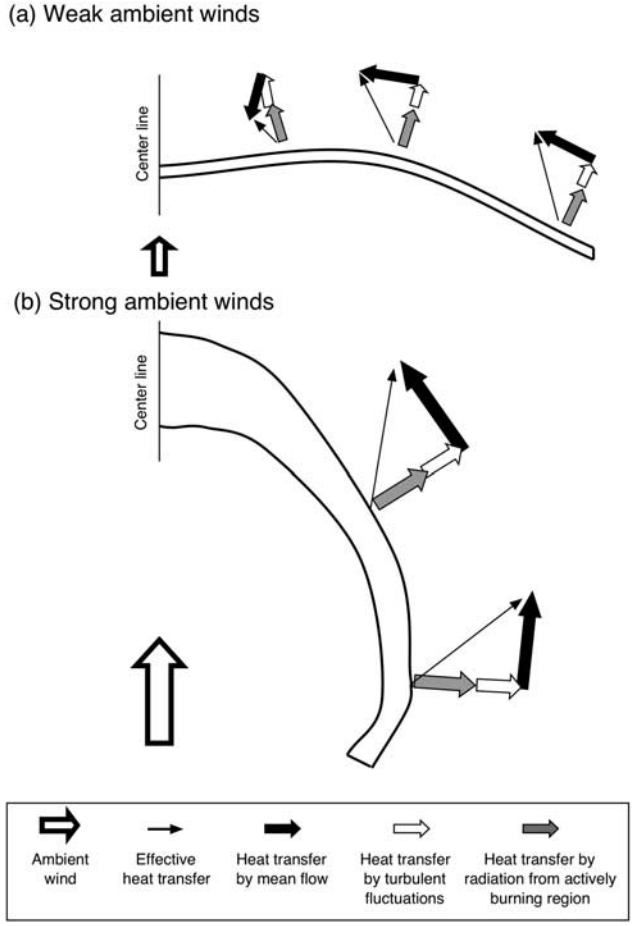

Figure 6. Schematic illustration of relative contributions of heat transfer by radiation (gray arrows), by mean flow advection (black arrows), and by turbulent advection (open arrows) to the total effective heat transfer (thin arrows) for (a) weak ambient winds, and (b) strong ambient winds. Only one half of the fire line is shown, and the arrow length indicates the relative intensity of the heat transfer.

fuel resulting from turbulence transport, and transfer of heat by mean-flow (i.e., resolved-flow) advection. Figure 6a depicts a portion of a fire line similar to those shown in Figures 1a and 1b, and is referred to as the weak wind example. In this schematic, a fire line that is far from parallel to the ambient flow is depicted. The direction of the mean-flow convection is indicated by the wind vectors in Figures 2a and 2b. The sum of these heat transfer processes produces a net effective heat transfer mechanism that moves energy downwind and obstructs lateral spread and the development of flanking fire lines.

[33] When referring to the schematic illustrations in Figures 6a and 6b it important to note that the turbulence transport flux refers to the combined effect of unresolved velocity fluctuations. This flux is treated as a diffusive process and is in general smaller than the flux due to heat being carried by the resolved flows. The resolved fluctuations are represented as part of the mean flow (i.e., the flow patterns that are represented in other figures with vectors). The net turbulent heat transport can then be in the opposite direction of the mean flow at that position.

[34] The schematic in Figure 6b depicts a portion of a fire line that is being driven by stronger winds than those associated with Figure 6a. The fire line in this case is oriented more closely parallel to the ambient wind than is that in Figure 6a. This fire line may be interpreted as being representative of the fires in Figures 1e, 1f, 1g, and 1h, and is referred to as the strong wind example. The three mechanisms of heat transfer that are described and shown in Figure 6a are also shown here with a resulting net effective heat transfer direction. The important difference between Figures 6a and 6b is that there is a component of the resulting heat transfer in the latter that feeds lateral spread of the fire along the flanking fire line (see Figure 3b, for example), whereas the mean flow actually works to obstruct the lateral spread of the fire in the former. This difference is primarily a result of the stronger influence that the fire has on the mean flow in the region of unburned fuel in the weak wind example. Another contributing factor is that the radiative heating and convection by turbulent fluctuations are weaker in the weak wind cases because of the narrower fire line, less intense fire, and weaker atmospheric turbulence. A quantitative analysis of this explanation will be given in future publications.

[35] In a more detailed analysis of the simulations, we now examine the dynamics of the simulated fires on a case-by-case basis. In comparing the short line cases, it can be seen that, in addition to the expected increase in downwind spread rate with increasing ambient wind speed, there is an increase in the lateral spread and in the extent of the flanking fire line. For weak ambient wind speeds (Figures 2a and 3a), the radiation and turbulent heat transfers from the relatively low intensity fire, which is shallow in the downwind direction, are not able to overcome the convective cooling on the flanks associated with the mean winds. Moreover, the fire-induced buoyancy column is strong in comparison to the near-surface ambient wind, such that the ambient flow is not redirected around the column, but rather becomes entrained into it. The increased entrainment into the column implies that less wind penetrates through the fire line, and thus there is less advective heat transfer downwind in the center of the fire line. Consequently, the head of the fire does not develop a pointed or conical leading edge (a process sometimes referred to as "necking").

[36] For stronger ambient winds, and most notably in the U12SHORT case (Figure 5a), there is more significant redirection of the ambient flow around the fire, thus further helping the fire to spread more in the lateral directions. This occurs because even though air is pulled into the base of the fire in all of the cases, at higher wind speeds there is more air being blown towards the hot region than can be entrained by the buoyant updraft. Some of the excess wind is redirected around the rising column, and other air that is carried towards the updraft finds ways to penetrate through the rising air, carrying heat with it towards unburned fuel. Furthermore, a stronger downwind component of hot plume motion enhances necking near the downwind edge of the fire. The increased penetration of the winds through the fireline and plume, more significant flanking fire lines, and converging winds at the downwind edge enhance the forward spread in that region.

[37] The fire behavior in the long line cases (Figures 2b, 3b, 4b, and 5b) displays several significant differences from

the behavior in the short line cases. The primary reason for this difference is that the convective column provides a wider obstruction to the ambient flow than it does in the short line cases, although the flows in these simulations are not analogous to flows around a solid obstacle since air from upstream can be entrained within, or pass through, the convective column. For weak ambient winds (U01LONG, Figure 2b), there is effectively no lateral spread for the reasons described above for the short line cases. Indeed, there is inward flow around much of the fire perimeter due both to low-level entrainment into the buoyant column and to the counter-rotating vortices found on the downwind side of the fire. Consequently, there is no flanking fire line and no lateral spread.

[38] The uneven downwind spread seen in the U01LONG case (Figure 2b), which is double-lobed or fingered, is caused by the counter-rotating vortex pair that results in a flow that is opposite in direction to the ambient wind at the downwind edge of the fire front. Entrainment requirements of the plume are not met by the upwind flow, therefore there is additional entrainment from the region downwind from the fire. This entrainment reduces the velocity in downwind direction, and in some locations reverses the flow in this region. For this ambient wind speed and length of fire line, this shape appears to be stable, since it persists with minimal variation for the duration of the simulation of more than 360 s.

[39] As the ambient wind speed increases, the persistent lobes seen in Figure 2b disappear. Instead, there are smaller-scale variations along the fire perimeter caused by instabilities (Figures 3b, 4b, and 5b). Based on their spatial scale (10–15 m, or 5–8 grid cells) and the fact that they can persist for up to 100 s, these instabilities appear to be caused by interactions between dynamical and physical processes, and not by numerical instabilities. It is noteworthy in this regard that the fire shapes in U03LONG, U06LONG, and U12LONG are relatively similar. In these simulations, winds near the ground are redirected around the fire perimeter as described above for the short line cases; even so, the stronger ambient winds, coupled with the presence of small-scale variations along the fire front, allows for increased flow through the convective column. Moreover, as with the short line cases, the lateral spread becomes more significant for higher ambient wind speeds. Since the fire is spreading rapidly in comparison to the characteristic burnout time of the solid fuel, the depth of the fire line is greater for higher ambient wind speeds. Consequently, the radiation from the fire line is more intense for stronger ambient winds, allowing for larger fire lines parallel to the flow on the flanks of the fire, and thus greater lateral spread.

[40] It is noted that the simulation of the U12LONG case (Figures 1h and 5b) exhibits greater intensity in the backing fire than do the simulations of the long-line cases with weaker ambient winds. This behavior is contrary to that seen in some actual fires [e.g., *Cheney and Gould*, 1995] and may be a result of the relatively low resolution of the fuel bed, since the drag induced by the fuel has a large effect on the convective heat transfer away from a backing fire. *Cheney and Sullivan* [1997] state that spread of the backing fire is essentially independent of wind speed in tall grasses, although it is possible to extinguish grass fires with very high winds directed towards the burnt area. This discrepancy between the simulations and field observations of fires could be caused by the relationship between the reaction rates and the turbulence, because turbulence levels are greater in the presence of high winds. It is also possible that the discrepancy might arise from the large number of simplifications made in the treatment of radiative heat transfer, since this is the main mode of heat transfer in the upwind direction for the high wind speed simulations. The ability of a backing fire to persist in tall grass is likely to be highly dependent on the velocity profile within the fuel bed and thus on the aerodynamic drag of the vegetation on the air moving through it. The model poorly resolves the velocity within the grass, which makes it difficult for the model to simulate the precise nature of the shelter that the unburned fuel gives to a weak backing fire in the low wind simulations and of the ability of wind to penetrate the top portion of the grass in the high wind simulations. This could cause the weak fires in the low wind cases to be blown out, or in the high wind cases to provide too much shelter for the backing fire and induce extra turbulence (thus increasing the intensity of the backing fire). This difference between simulated results and field experiments requires examination in future research. In this regard, it is noteworthy that although the bulk fuel density is taken to be uniform within the fuel bed in the simulations, in reality grass fuel beds typically have a bulk density that is greatest near the base and that decreases with height. Since it is typically observed that backing and flank fires are supported by combustion in the higher density portion of the fuel bed nearer the ground, it is possible that poor resolution of the fuel bed itself may be responsible for some of the differences between simulated and observed fire behavior and the back and flanks of the fire.

[41] It is worth noting that the length-to-breadth ratios of the fires in the high wind cases appear to be smaller than would be expected from observations of fires. In this regard, *Alexander* [1985] suggests that for winds of 12 m s^{-1} this ratio is approximately 6 to 1. This ratio applies to a point ignition source, however, while the simulated fires start from lines of finite width. It can be verified by inspection of Figure 5 that the ratio of the spread from the original fire line in the downwind direction to the spread in the lateral direction is about 5 to 1 in the short line case and about 6 to 1 in the long line case. If the fires were allowed to burn for longer times to larger sizes, the overall shape ratios might approach those of a point fire as the initial line length becomes much smaller compared to the distance that the fire traveled.

[42] Figure 7 depicts the ratio of the vertical velocity, w, to the inlet wind speed, U_{in}, for U01LONG, U03LONG, and U06LONG at $z = 2.26$ m and at $z = 3.78$ m (U12LONG is not shown because the ratio is uniformly small, and does not provide insight beyond that obtained by U06LONG). This ratio provides a measure of the relative strength of the convective column directly above the fuel bed in comparison to the ambient horizontal winds. Also shown in Figure 7 are the wind vectors and potential temperature contours at $z = 2.26$ m. These contours are given in order to illustrate the location of the hot regions in relation to the vertical motions.

[43] It is immediately apparent from this figure that for weak ambient winds the ratio is large, such that the vertical

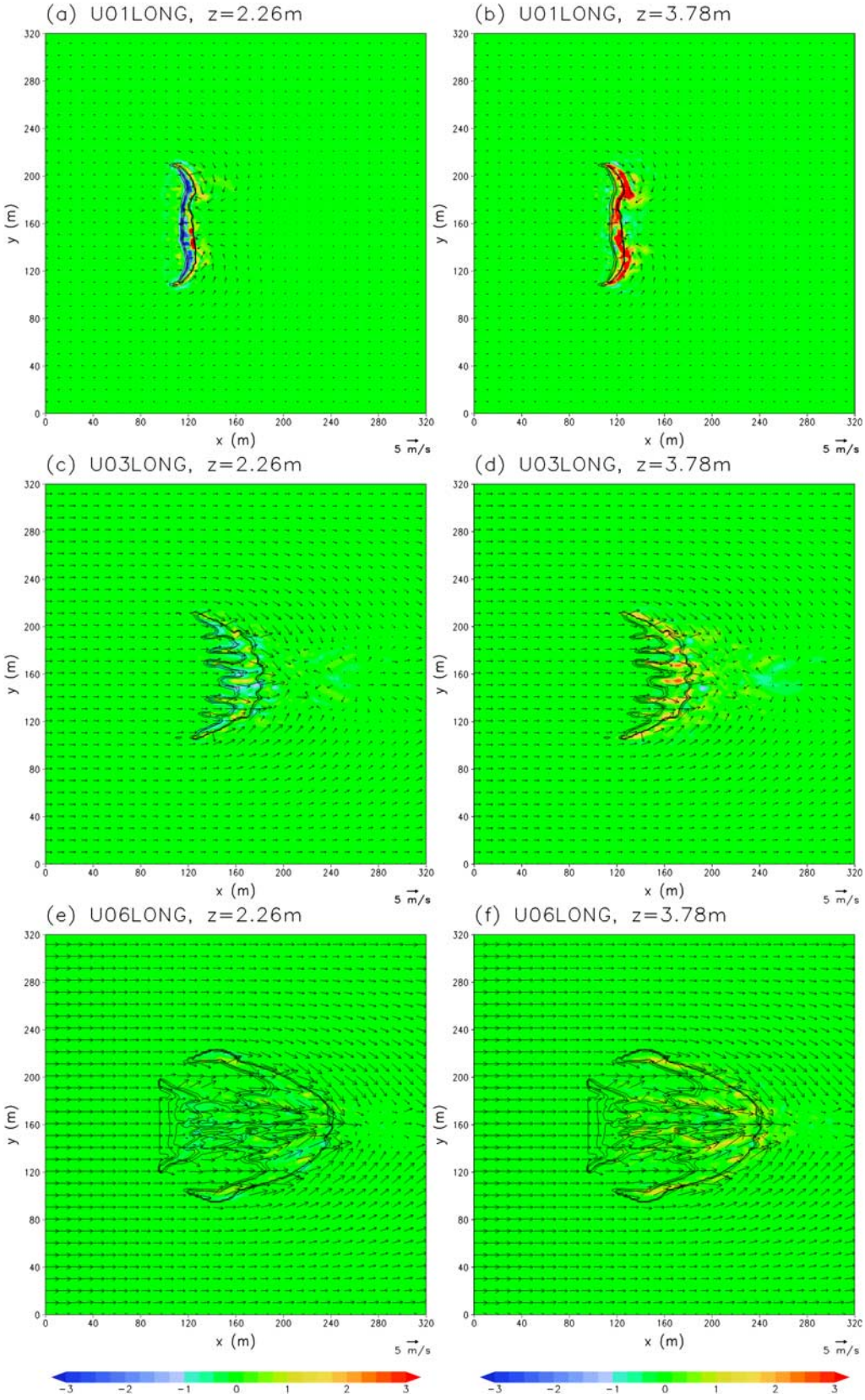

Figure 7. Horizontal cross sections of w/U_{in} (shaded as indicated) and potential temperature (solid lines at 400 K, 500 K, and 600 K) at t = 100 s for (a) U01LONG at z = 2.26 m, (b) U01LONG at z = 3.78 m, (c) U03LONG at z = 2.26 m, (d) U03LONG at z = 3.78 m, (e) U06LONG at z = 2.26 m, and (f) U06LONG at z = 3.78 m. Also shown are horizontal wind vectors at z = 2.26 m for t = 100 s (vectors plotted every 10 m).

motions in the convective column dominate the horizontal motions, whereas for stronger ambient winds the ratio is significantly smaller, and the flow is primarily horizontal. Moreover, the spatial structure of this ratio is also highly dependent on the ambient wind speed. For the U01LONG case (Figures 7a and 7b), it is evident that the vertical motions are relatively uniform along the fire line, although there is some flow through the column at several locations. The strongest vertical motion seen at $z = 2.26$ m (Figure 7a) is downward and located behind the fire line, where the vegetation density is significantly reduced. This downward flow augments the ambient wind in feeding the base of the buoyant column which forms above the hot region (Figure 7b). There is no equivalent downdraft downwind of the fire because of the ambient wind and vegetation drag that exists there. The buoyant column over the hot region is not as intense at $z = 2.26$ m because the upward moving air above the fire has had little time to accelerate, whereas at $z = 3.78$ m the vertical motion is predominantly upward. For the U03LONG case (Figures 7c and 7d), the ratio is slightly smaller, but more noteworthy in this case is the fact that the vertical motion is more variable along the fire line, and this is particularly evident at $z = 3.78$ m (Figure 7d). Moreover, the along-line variations in vertical motion correlate well with variations in the potential temperature (and, as can be seen in Figure 7b, with variations in fire spread as well). As noted previously, these along-line variations are indicative of the presence of significant flow through the fire line, and of self-sustaining vorticity structures.

[44] As the ambient wind increases further still (U06LONG, Figures 7e and 7f), the vertical velocity becomes much smaller in comparison to the ambient horizontal winds, the impact of the convective column on fire spread diminishes, and the fire front progresses in a relatively smooth and uniform manner. It is probably not coincidental, then, that it is the high wind cases that resemble most closely the characteristic shape of wind-driven fires described by *Anderson* [1983]. Also apparent in Figures 7e and 7f is that the air near the ground is still relatively hot upwind of the fire front, indicating that there are still regions of actively burning fuel well upstream of the fire front.

[45] In an effort to understand further the vertical motion patterns seen in Figure 7, Figure 8 displays the wind vectors in the x–z plane 28 m from the centerline for the U01LONG case (Figure 8a) and the U03LONG case (Figure 8b). The 350 K contour of potential temperature is also displayed in each panel to illustrate the location of the hot air in the plume. For weak winds (U01LONG, Figure 8a), it is apparent that vertical motion dominates horizontal motion, as indicated in Figures 7a and 7b, with the strongest upward motion above and downwind of the fire front within the plume. The downward motion near the ground evident in Figure 7a appears to arise as part of a horizontal vortex centered immediately upstream of the fire front, similar to the vortex structures seen in the numerical simulations described by *Heilman and Fast* [1992] and *Cunningham et al.* [2005]. There is also evidence of a weaker horizontal vortex downstream of the fire. In Figure 8a, the lower portion of the vortex located just upstream of the fire is part of the indraft. This flow feature further illustrates the accelerated winds that occur behind the fire where the vegetation has been depleted. For stronger winds (U03LONG, Figure 8b), the horizontal component of the wind is clearly more significant, the increased flow through the fire line immediately above the fuel bed is apparent, and the presence of horizontal vortices is less obvious.

[46] By way of summarizing the foregoing discussion, Figure 9 illustrates the downwind propagation of the fire front with time for all eight simulations. The spread rate can be seen to be nearly constant in all cases, with the slight exception of the period between 100 s and 200 s for the U06SHORT case. A linear fit to each of these curves provides a representative measure of the spread rate, and the rates so obtained are given in Table 2.

4. Comparison of Simulations With Empirical Fire Spread Models

[47] Empirical models of fire spread are useful tools for fire managers, and in this regard several different models are in use throughout the world for operational wildfire prediction. The most widely used tool in the United States is based on the empirical equations described by *Rothermel* [1972]. These empirical equations form the foundation for the spread rate calculations in the BEHAVE [*Andrews et al.*, 2003] and FARSITE [*Finney*, 1998] models, and were developed based on data from a variety of fires burning on constant slopes, constant winds, and homogeneous fuels. In Australia, the basis for operational prediction of grass fire spread is the model described by *Cheney et al.* [1998]. The empirical equations that constitute this model are based on data both from large experimental fires and from wildfires.

[48] It is useful to compare the downwind (i.e., head fire) spread rates from the HIGRAD/FIRETEC simulations described in the previous section to the spread rates obtained from these empirical models for similar fuel and environmental parameters, because these models were derived directly from data, and because these spread rates are familiar to the respective wildfire communities. Nevertheless, it is difficult to perform simulations for identical conditions because the input variables and the level of detail are significantly different for each model; thus the fuel, boundary, and initial conditions are difficult to match between the models. Moreover, as will be discussed in more detail below, the manner in which the two empirical models describe the relationship between the rate of spread of the fire and the ambient atmospheric wind speed is different.

[49] For the present study, we employ the BEHAVE model implementation of Rothermel's equations, which require as input the ambient wind at a level referred to as the "mid-flame height". This wind is intended to represent the environmental wind that is affecting the fire, and thus should be measured away from the influence of the fire. To compare the spread rates seen in the simulated fires with those predicted from Rothermel's equations, we characterize each simulation in terms of a non-fire-influenced simulated mid-flame wind speed, which will in general be different from the assigned inlet wind speed because of drag near the surface. To determine this simulated mid-flame wind speed for a given ambient wind, the HIGRAD/FIRETEC model is run for each inlet wind speed without the fire until a steady-state wind profile is obtained. The ambient wind at any model level can then be obtained directly. Since we do not

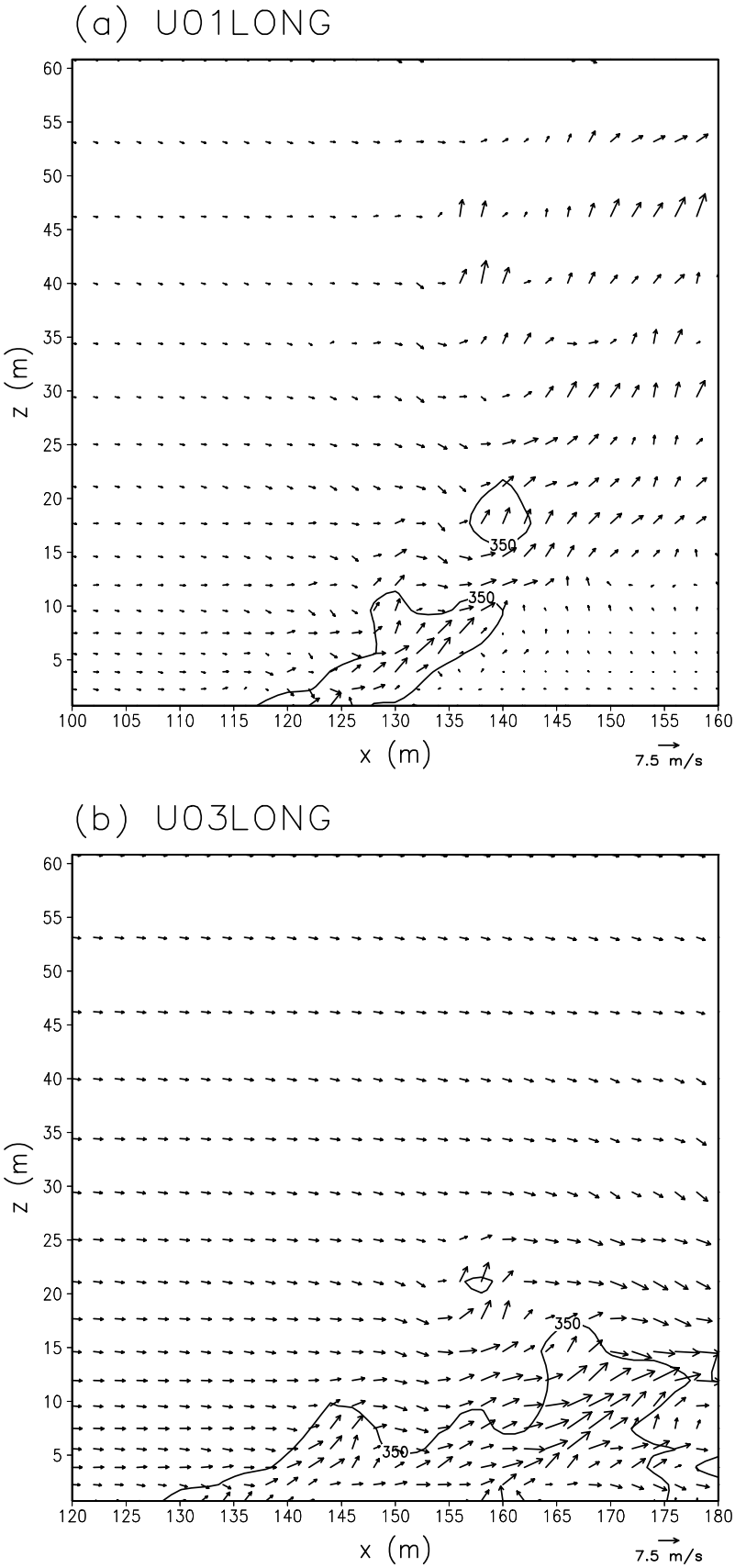

Figure 8. Vertical cross section, taken at 28 m in the positive *y*-direction from the center line, of potential temperature (thin solid line at 350 K) and wind vectors in the plane of the cross section at t = 100 s for (a) U01LONG and (b) U03LONG.

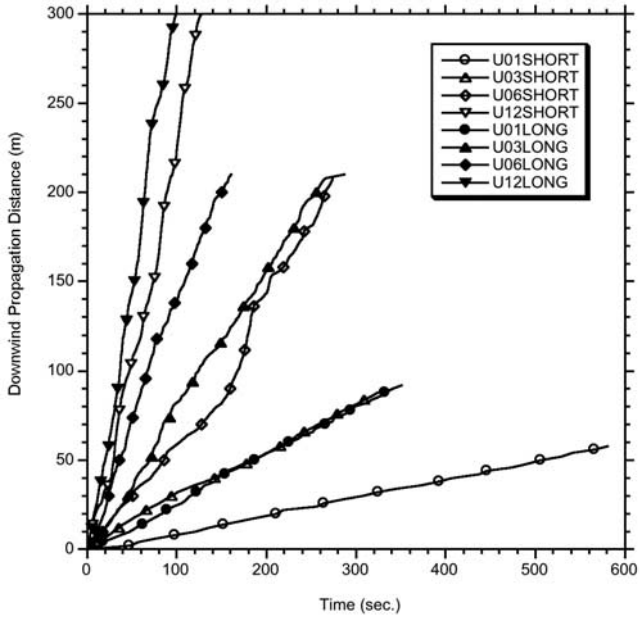

Figure 9. Downwind propagation distance as a function of time for all eight simulations.

know specifically at which model level the mid-flame height should be specified, we examine the possibility of using either $z = 2.26$ m or $z = 3.78$ m (i.e., the centers of the first two computational cells that are entirely above the fuel bed) to define this height. Although flame height is difficult to measure accurately in wildfires due to the highly variable nature of the flames, for the range of ambient wind speeds studied here, typical values for flame heights in grass fires range from about 2–3 m for weak winds to about 8 m for strong winds. Consequently, it is suggested that the heights used for this purpose in the model are appropriate. The empirical model described by *Cheney et al.* [1998] takes as input the wind speed measured at the standard anemometer height of 10 m above the ground; the ambient wind obtained from the HIGRAD/FIRETEC model at this height is essentially equal to the inlet wind speed.

[50] The HIGRAD/FIRETEC simulated spread rate for each case is plotted in Figure 10 (circles for the short line cases and triangles for the long line cases), along with the calculations obtained from the BEHAVE model for two different mid-flame wind speeds (Figures 10a and 10b) and from the model due to *Cheney et al.* [1998] (Figure 10c). Figure 10a shows the comparison of HIGRAD/FIRETEC simulated spread rates to BEHAVE spread rates when the

Table 2. Simulated Fire Spread Rates

Simulation	Ambient Wind Speed, U_{in}, m s^{-1}	Spread Rate, m s^{-1}
U01SHORT	1.0	0.10
U01LONG	1.0	0.27
U03SHORT	3.0	0.26
U03LONG	3.0	0.79
U06SHORT	6.0	0.76
U06LONG	6.0	1.37
U12SHORT	12.0	2.41
U12LONG	12.0	3.22

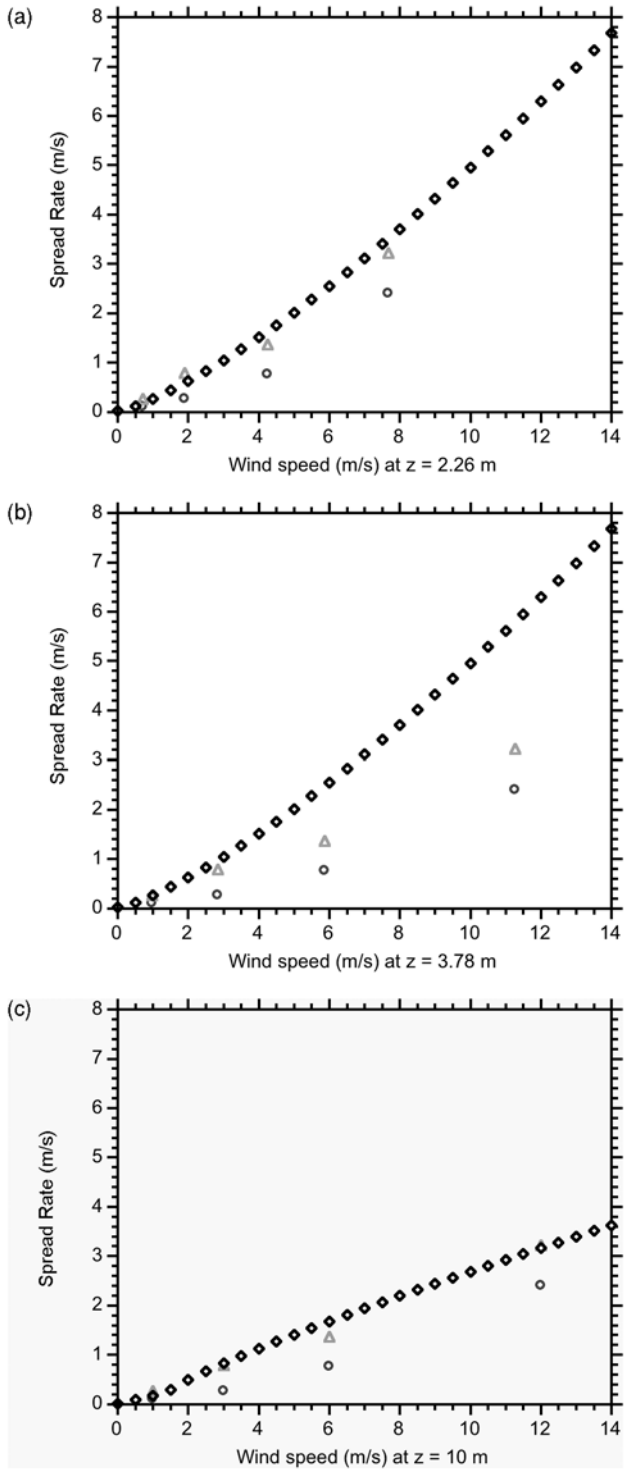

Figure 10. Comparison of FIRETEC simulated spread rates (triangles, long line cases; circles, short line cases) with spread rates obtained from empirical fire spread models (diamonds) as a function of wind speed. (a) Spread rates from BEHAVE model due to *Rothermel* [1972] with wind speeds taken from FIRETEC at $z = 2.26$ m; (b) spread rates from BEHAVE model with wind speeds taken from FIRETEC at $z = 3.78$ m; and (c) spread rates from model due to *Cheney et al.* [1998] with wind speeds taken from FIRETEC at $z = 10$ m.

wind at $z = 2.26$ m in the simulation is taken to be the mid-flame wind speed, while Figure 10b shows the comparison when the wind at $z = 3.78$ m in the simulation is taken to be the mid-flame wind speed. The BEHAVE spread rates are identical in both panels because they depend only on the magnitude of the mid-flame wind speed, not on the height at which this wind speed is measured. The fuel input to the BEHAVE model corresponds to the so-called "Fuel Model 3" [*Anderson*, 1982], which is representative of tall grass, and the moisture fraction is taken to be equal to 0.05. It is apparent from this figure that the closest correspondence between the simulated spread rates and the BEHAVE model calculations is obtained for the long fire lines when the fire is characterized by the ambient winds at $z = 2.26$ m. On the other hand, if the wind at $z = 3.78$ m is used to specify the mid-flame wind speed, the corresponding spread rate obtained from the BEHAVE model is approximately twice that simulated by HIGRAD/FIRETEC.

[51] Two important implications arise from consideration of this figure. The first is that fire line length is important, and so by implication is the shape and size of the fire, and caution should be advised in assigning a BEHAVE spread rate value simply based on the mid-flame wind speed. The second is that the spread rate can be highly sensitive to the value chosen for the mid-flame wind speed (or more simply what height is used to measure wind speed). Since in general there will be considerable vertical wind shear near the ground, the spread rate obtained from an empirical model such as BEHAVE may overestimate (or underestimate) significantly the actual spread rate depending on which level is chosen as the mid-flame height. An additional level of uncertainty may arise in this regard if the available wind speed measurements are given at different levels, in which case they must be adjusted to the mid-flame height via an anticipated wind profile (e.g., a logarithmic profile in a neutrally stratified surface layer).

[52] For the comparison of the simulated spread rates with the empirical model of *Cheney et al.* [1998] shown in Figure 10c, we employ the equations for spread rate in the latter that are appropriate for grass in a natural pasture, with a fuel moisture content of 0.05. It is apparent from this figure that the HIGRAD/FIRETEC simulated spread rates for the long line cases are very close to the predictions from the empirical model under these conditions. This result is encouraging with respect to the relevance of the simulations because the empirical model described by *Cheney et al.* [1998] is based on field experiments of grass fires, whereas the model described by *Rothermel* [1972] is based primarily on scale experiments in a laboratory wind tunnel. Moreover, the former model does not appear to suffer from the uncertainty associated with the latter model discussed above concerning the definition of a mid-flame height, or the interpolation to this height of winds measured at a different level.

[53] It is noteworthy that the relationship between spread rate and wind speed is different for the two empirical models, but that the trends that these two models display in this regard are both similar to those simulated by HIGRAD/FIRETEC, particularly for the long line cases (see Figures 10a and 10c). Both empirical models exhibit a power-law dependence between spread rate and wind speed; the BEHAVE model assumes the associated exponent is greater than unity for long grass, whereas *Cheney et al.* [1998] found that a value slightly less than unity was the best fit to their experimental data for ambient wind speeds greater than 2.2 m s^{-1} (for wind speeds less than 2.2 m s^{-1} the relationship is taken to be linear). It is also important to note that these exponents are used to relate different winds (i.e., at "mid-flame height" in the BEHAVE model and at 10 m in the model of *Cheney et al.* [1998]) to the spread rate, and the relationship between the winds at these two different heights is likely to be different since the relationship between the winds at the various heights is not linear. As discussed both by *Beer* [1993] and by *Cheney et al.* [1998], several different power-law relationships have been proposed in the literature on fire spread; however, it is not obvious which, if any, is appropriate, and other factors not considered here such as atmospheric stability may complicate the issue further [e.g., *Beer*, 1991]. Indeed, *Beer* [1991] suggests that there may be no unique or simple functional dependence of the spread rate on the wind speed. Although simulations from coupled atmosphere–fire models may be able to shed some light on the fundamental dynamics relating the fire spread to the ambient wind, to address the nature of any empirical relationship between these quantities would require a much larger number of simulations than is shown here, and as such is beyond the scope of the present study.

5. Conclusions

[54] In this paper, a coupled atmosphere–fire model has been employed to explore several fundamental aspects of fire behavior, and specifically the dependence of this behavior on the ambient atmospheric winds and the initial length of the fire line. This model is based on a multi-phase transport approach, and incorporates representations of the physical processes that govern wildfires such as combustion, turbulence, and radiative and convective heat exchange.

[55] As anticipated from observational evidence, the forward spread of the simulated fires (i.e., the spread of the fire in the direction of the ambient wind) increases with ambient wind speed. However, the forward spread also depends significantly on the initial length of the fire line, such that for a given ambient wind speed the spread rate for long lines is greater than that for short lines. This result is consistent with the experimental fires investigated by *Cheney et al.* [1993] and *Cheney and Gould* [1995] (for graphic evidence of this behavior, see the photograph shown in Figure 4.4 of *Cheney and Sullivan* [1997]). Additionally, the lateral spread of the simulated fires depends on the ambient wind speed and the length of the fire line.

[56] Consequently, not only does the spread rate of the fires depend on the ambient wind, but so also does the overall shape and size of the fire. It is particularly noteworthy in this regard that for weak ambient winds, the shape of the fire perimeter is dramatically different from that seen in the higher wind speed simulations. This difference is attributed to the differences in the nature of the coupled atmosphere–fire interactions between the low wind speed and high wind speed cases, such as the increased ability for the wind to penetrate through the plume with increased

winds. This coupling between the atmosphere and the fire is complex, but can be understood in terms of the interplay between radiative and convective heat transfer. The nature of this interplay between various radiative and convective heat transfer mechanisms, the effect this has on the coupling between the fire and the atmosphere, and its impact on fire behavior will be explored in more detail in future research.

[57] Finally, it is noteworthy that the trends of spread rates and fire behavior simulated by the model are consistent with those observed in the field experiments described by *Cheney et al.* [1993] and *Cheney and Gould* [1995], and indeed the simulated head fire spread rates are very close to those predicted by the empirical model proposed by *Cheney et al.* [1998] that is based on these experiments. Significant differences do exist, however, and the details of fire spread at the flanks and the back of the fire exhibit some differences from observations of grass fires. These discrepancies may result from overly simplified treatments of radiation or turbulent heat exchange, or under-resolution of the fuel bed, and remain aspects of the model that may require further development.

Appendix A: Governing Equations of the FIRETEC Model

[58] The simplified reaction used in the FIRETEC model is described by

$$N_f(\text{fuel}) + N_o(\text{oxygen}) \rightarrow (\text{products}) + (\text{heat}), \tag{A1}$$

where N_f and N_o are the stoichiometric coefficients for fuel and oxygen, respectively.

[59] The equations for the solid phase express the conservation of fuel, moisture and energy, and are written in terms of averaged properties of physical quantities in a resolved volume as follows:

$$\frac{\partial \rho_f}{\partial t} = -N_f F_f, \tag{A2}$$

$$\frac{\partial \rho_w}{\partial t} = -F_w, \tag{A3}$$

$$\begin{aligned}\left(c_{p_f}\rho_f + c_{p_w}\rho_w\right)\frac{\partial T_s}{\partial t} &= Q_{rad,s} + h a_v\left(T_g - T_s\right) \\ &- F_w\left(H_w + c_{p_w}T_{vap}\right) + F_f\left(\Theta H_f - c_{p_f}T_{pyr}N_f\right).\end{aligned} \tag{A4}$$

[60] Here, ρ_f and ρ_w are the bulk densities of solid fuel and liquid water, respectively, F_f and F_w are respectively the reaction rates for solid fuel (vegetation) and liquid water depletion (i.e., the evaporation rate), c_{p_f} and c_{p_w} are the specific heats at constant pressure of the fuel and water, respectively, T_s is the temperature of the solid fuel, $Q_{rad,s}$ is the net thermal radiation heat flux to the solid, h is the convective heat transfer coefficient, a_v is the ratio of the surface area of the fuel to the resolved volume (surface area per unit volume of fuel times the volume fraction), T_g is the temperature of the combined gas, H_w is the heat energy per unit mass associated with liquid water evaporation, T_{vap} is the temperature at which the liquid water evaporates, H_f is the heat energy per unit mass associated with the reaction (A1), Θ is the fraction of heat released from the combined solid–gas reaction that is deposited directly back into the solid (see *Linn et al.* [2002] for more details), and T_{pyr} is the temperature at which the solid fuel begins to pyrolyze.

[61] The equations for the gas phase express the conservation of mass, momentum, energy, and species (i.e., oxygen), as follows:

$$\frac{\partial \rho_g}{\partial t} + \frac{\partial}{\partial x_j}\left(\rho_g u_j\right) = N_f F_f + F_w, \tag{A5}$$

$$\frac{\partial}{\partial t}\left(\rho_g u_i\right) + \frac{\partial}{\partial x_j}\left(\rho_g u_i u_j\right) + \frac{\partial p}{\partial x_i} - \rho_g g_i = -\frac{\partial R_{ij}}{\partial x_j} - \rho_g C_D a_v |u| u_i, \tag{A6}$$

$$\begin{aligned}\frac{\partial}{\partial t}\left(\rho_g \theta\right) + \frac{\partial}{\partial x_j}\left(\rho_g \theta u_j\right) &= \frac{\partial}{\partial x_j}\left(\sigma \frac{\partial \theta}{\partial x_j}\right) \\ &+ \frac{\theta}{c_p T_g}\left[h a_v\left(T_s - T_g\right) + Q_{rad,g} + (1-\Theta)F_f H_f\right],\end{aligned} \tag{A7}$$

$$\frac{\partial \rho_o}{\partial t} + \frac{\partial}{\partial x_j}\left(\rho_o u_j\right) = \frac{\partial}{\partial x_j}\left[\sigma \frac{\partial}{\partial x_j}\left(\frac{\rho_o}{\rho_g}\right)\right] - N_o F_f. \tag{A8}$$

[62] In these equations, ρ_g is the combined gas density, u_i is the combined gas velocity where $i = 1$, 2, or 3 represents the velocity component in the x, y, or z direction, g_i is the gravitational acceleration in the i direction, R_{ij} is the turbulent Reynolds stress tensor, C_D is the vegetation drag coefficient, θ is the potential temperature of the combined gas, σ is the turbulent diffusion coefficient, c_p is the specific heat at constant pressure of the combined gas, $Q_{rad,g}$ is the net thermal radiation heat flux to the gas, and ρ_o is the density of oxygen.

Appendix B: Representation of the Turbulent Velocity Correlations and the Turbulent Diffusion

[63] Turbulence is represented in the FIRETEC model as the sum of three separate turbulence spectra corresponding to scales of sizes A, B, and C. Contributions to the Reynolds stress tensor, R_{ij}, from each of these scales are represented respectively by $R_{ij,A}$, $R_{ij,B}$, and $R_{ij,C}$, such that

$$R_{ij} = R_{ij,A} + R_{ij,B} + R_{ij,C}. \tag{B1}$$

[64] For the A scales, a point functional relationship is assumed between the Reynolds stress tensor, $R_{ij,A}$, and the turbulent kinetic energy, $K_A = R_{ii,A}/2\rho_g$, as follows

$$R_{ij,A} = -\rho_g \nu_t\left(\frac{\partial u_i}{\partial x_j} + \frac{\partial u_j}{\partial x_i}\right) + \frac{2}{3}\delta_{ij}\left(\rho_g \nu_t \frac{\partial u_k}{\partial x_k} + \rho_g K_A\right), \tag{B2}$$

where ν_t is the turbulent viscosity. A transport equation for K_A is then required, and is given by

$$\begin{aligned}\frac{\partial}{\partial t}\left(\rho_g K_A\right) + \frac{\partial}{\partial x_i}\left(\rho_g K_A u_i\right) &= -R_{il,A}\frac{\partial u_i}{\partial x_l} + \frac{2}{3}C_{DR}\frac{\partial}{\partial x_l}\left(s_A \frac{R_{lk}}{K^{1/2}}\frac{\partial K_A}{\partial x_k}\right) \\ &- \frac{K^{1/2}}{s_A}K_A - \rho_g C_D a_{v,B} K^{1/2} K_A,\end{aligned} \tag{B3}$$

where C_{DR} is a constant, s_A is the characteristic size of the A scales, $a_{v,B}$ is the surface area to volume ratio of the B scale fuels, and $K = K_A + K_B + K_C$.

[65] Equations for the B scales are similar to those employed for the A scales. Specifically, the Reynolds stress tensor is given by

$$R_{ij,B} = -\rho_g \nu_t \left(\frac{\partial u_i}{\partial x_j} + \frac{\partial u_j}{\partial x_i} \right) + \frac{2}{3} \delta_{ij} \left(\rho_g \nu_t \frac{\partial u_k}{\partial x_k} + \rho_g K_B \right), \quad \text{(B4)}$$

where $K_B = R_{ii,B}/2\rho_g$, and the transport equation for K_B is given by

$$\frac{\partial}{\partial t}\left(\rho_g K_B\right) + \frac{\partial}{\partial x_i}\left(\rho_g K_B u_i\right) = -R_{il,B}\frac{\partial u_i}{\partial x_l} + \frac{2}{3} C_{DR} \frac{\partial}{\partial x_l}\left(s_B \frac{R_{lk}}{K^{1/2}} \frac{\partial K_B}{\partial x_k} \right) - \frac{K^{1/2}}{s_B} K_B - \rho_g C_D a_{v,C} K^{1/2} K_B + \rho_g C_D a_{v,B}\left(K^{1/2} K_A + |u|^3 \right). \quad \text{(B5)}$$

Here, s_B is the characteristic size of the B scales, and $a_{v,C}$ is the surface area to volume ratio of the C scale fuels.

[66] It is possible to apply similar equations for the C scales also; however, since it is expected that the locations where turbulence on the C scales is created are statistically in the same vicinity as the locations where turbulence on the B scales is created (i.e., in the fuel bed), $R_{ij,C}$ is taken to be proportional to $R_{ij,B}$.

[67] Finally, the turbulent diffusion coefficient is taken to be

$$\sigma = 0.09 \rho_g s_B K_B^{1/2}. \quad \text{(B6)}$$

[68] **Acknowledgments.** We thank Francis H. Harlow for a detailed review of this paper and extensive discussions on the subject matter. Discussions with Scott Goodrick and Jon Reisner were also particularly valuable. We thank Phil Cheney and two anonymous reviewers for numerous comments on the original version of the manuscript that helped clarify the presentation of the results. Portions of this work were supported by the USDA Forest Service Rocky Mountain Research Station, Pacific Southwest Research Station, and Southern Research Station, under the direction of Carleton Edminster, David Weise, and Scott Goodrick.

References

Alexander, M. E. (1985), Estimating the length-to-breadth ratio of elliptical forest fire patterns, in *Proceedings of the Eighth Conference on Fire and Forest Meteorology*, edited by L. R. Donoghue and R. E. Martin, pp. 287–304, Soc. of Am. For., Bethesda, Md.

Anderson, H. E. (1982), Aids to determining fuel models for estimating fire behavior, *Gen. Tech. Rep. INT-122*, 22 pp., U.S. Dep. of Agric. For. Serv., Ogden, Utah.

Anderson, H. E. (1983), Predicting wind-driven wild land fire size and shape, *Res. Pap. INT-305*, 26 pp., U.S. Dep. of Agric. For. Serv., Ogden, Utah.

Andrews, P. L., C. D. Bevins, and R. C. Seli (2003), BehavePlus fire modeling system, version 2.0: User's guide, *Gen. Tech. Rep. RMRS-GTR-106WWW*, 132 pp., U.S. Dep. of Agric. For. Serv., Ogden, Utah.

Beer, T. (1991), The interaction of wind and fire, *Boundary Layer Meteorol.*, *54*, 287–308.

Beer, T. (1993), The speed of a fire front and its dependence on wind speed, *Int. J. Wildland Fire*, *3*, 193–202.

Burgan, R. E. (1988), Revisions to the 1978 National Fire-Danger Rating System, *Res. Pap. SE-273*, 39 pp., U.S. Dep. of Agric. For. Serv., Asheville, N. C.

Carrier, G. F., F. E. Fendell, and M. F. Wolff (1991), Wind-aided firespread across arrays of discrete fuel elements, I. Theory, *Combust. Sci. Tech.*, *75*, 31–51.

Catchpole, W. R., E. A. Catchpole, B. W. Butler, R. C. Rothermel, G. A. Morris, and D. J. Latham (1998), Rate of spread of free- burning fires in woody fuels in a wind tunnel, *Combust. Sci. Tech.*, *131*, 1–37.

Cheney, N. P., and J. S. Gould (1995), Fire growth in grassland fuels, *Int. J. Wildland Fire*, *5*, 237–244.

Cheney, N. P., and A. Sullivan (1997), *Grassfires: Fuel, Weather and Fire Behaviour*, 112 pp., CSIRO, Collingwood, Victoria, Australia.

Cheney, N. P., J. S. Gould, and W. R. Catchpole (1993), The influence of fuel, weather and fire shape variables on fire-spread in grasslands, *Int. J. Wildland Fire*, *3*, 31–44.

Cheney, N. P., J. S. Gould, and W. R. Catchpole (1998), Prediction of fire spread in grasslands, *Int. J. Wildland Fire*, *8*, 1–13.

Clark, T. L., M. A. Jenkins, J. L. Coen, and D. R. Packham (1996a), A coupled atmosphere–fire model: Convective feedback on fire line dynamics, *J. Appl. Meteorol.*, *35*, 875–901.

Clark, T. L., M. A. Jenkins, J. L. Coen, and D. R. Packham (1996b), A coupled atmosphere–fire model: Role of the convective Froude number and dynamic fingering at the fireline, *Int. J. Wildland Fire*, *6*, 177–190.

Clark, T. L., M. Griffiths, M. J. Reeder, and D. Latham (2003), Numerical simulations of grassland fires in the Northern Territory, Australia: A new subgrid-scale fire parameterization, *J. Geophys. Res.*, *108*(D18), 4589, doi:10.1029/2002JD003340.

Clark, T. L., J. L. Coen, and D. Latham (2004), Description of a coupled atmosphere–fire model, *Int. J. Wildland Fire*, *13*, 49–63.

Cunningham, P., S. L. Goodrick, M. Y. Hussaini, and R. R. Linn (2005), Coherent vortical structures in numerical simulations of buoyant plumes from wildland fires, *Int. J. Wildland Fire*, *14*, 61–75.

Drysdale, D. (1998), *An Introduction to Fire Dynamics*, 2nd ed., 470 pp., John Wiley, Hoboken, N. J.

Finney, M. A. (1998), FARSITE: Fire Area Simulator—Model development and evaluation, *Res. Pap. RMRS-RP-4*, 47 pp., U.S. Dep. of Agric. For. Serv., Ogden, Utah.

Fons, W. T. (1946), Analysis of fire spread in light forest fuels, *J. Agric. Res.*, *72*, 93–121.

Grishin, A. M. (1997), *Mathematical Modeling of Forest Fires and New Methods of Fighting Them*, edited by F. A. Albini, 390 pp., Tomsk State Univ., Tomsk, Russia.

Heilman, W. E., and J. D. Fast (1992), Simulations of horizontal roll vortex development above lines of extreme surface heating, *Int. J. Wildland Fire*, *2*, 55–68.

Larini, M., F. Giroud, B. Porterie, and J.-C. Loraud (1998), A multiphase formulation for fire propagation in heterogeneous combustible media, *Int. J. Heat Mass Transf.*, *41*, 881–897.

Linn, R. R. (1997), A transport model for prediction of wildfire behavior, *Sci. Rep. LA-13334-T*, 195 pp., Los Alamos Natl. Lab., Los Alamos, N. M.

Linn, R. R., and F. H. Harlow (1998), Mixing-limited transport model used for description of wildfires, in *Computational Technologies for Fluid/Thermal/Structural/Chemical Systems With Industrial Applications*, PVP-vol. 377-2, edited by C. R. Kleijn, S. Kawano, and V. V. Kudriavtsev, pp. 161–168, Am. Soc. of Mech. Eng., New York.

Linn, R. R., J. M. Reisner, J. J. Colman, and J. Winterkamp (2002), Studying wildfire behavior using FIRETEC, *Int. J. Wildland Fire*, *11*, 233–246.

Morvan, D., and J.-L. Dupuy (2001), Modeling of fire spread through a forest fuel bed using a multiphase formulation, *Combust. Flame*, *127*, 1981–1994.

Porterie, B., D. Morvan, J.-C. Loraud, and M. Larini (2000), Firespread through fuel beds: Modeling of wind-aided fires and induced hydrodynamics, *Phys. Fluids*, *12*, 1762–1782.

Rehm, R. G., D. D. Evans, W. E. Mell, S. Hostikka, K. B. McGrattan, G. P. Forney, C. Bouldin, and E. Baker (2003), Neighborhood-scale fire spread, paper presented at 5th Symposium on Fire and Forest Meteorology, Am. Meteorol. Soc., Orlando, Fla., 16–20 Nov.

Reisner, J. M., S. Wynne, L. Margolin, and R. R. Linn (2000), Coupled atmospheric–fire modeling employing the method of averages, *Mon. Weather Rev.*, *128*, 3683–3691.

Rothermel, R. C. (1972), A mathematical model for predicting fire spread in wildland fuels, *Res. Pap. INT-115*, 40 pp., U.S. Dep. of Agric. For. Serv., Ogden, Utah.

Sneeuwjagt, R. J., and W. H. Frandsen (1977), Behavior of experimental grass fires vs. predictions based on Rothermel's fire model, *Can. J. For. Res.*, *7*, 357–367.

Stephens, G. L. (1984), The parameterization of radiation for numerical weather prediction and climate models, *Mon. Weather Rev.*, *112*, 827–867.

Weise, D. R. (1993), Modelling wind and slope-induced wildland fire behavior, Ph.D. dissertation, 130 pp., Univ. of Calif., Berkeley.

Wilson, C. C., and J. C. Sorenson (1978), Some common denominators of fire behavior on tragedy and near-miss forest fires, *Publ. NA-GR-8*, 31 pp., U.S. Dep. of Agric. For. Serv., Broomall, Pa.

Wolff, M. F., G. F. Carrier, and F. E. Fendell (1991), Wind-aided firespread across arrays of discrete fuel elements. II. Experiment, *Combust. Sci. Tech.*, *77*, 261–289.

P. Cunningham, Department of Meteorology and Geophysical Fluid Dynamics Institute, Florida State University, Tallahassee, FL 32306-4520, USA. (cunningham@met.fsu.edu)

R. R. Linn, Earth and Environmental Sciences Division, Los Alamos National Laboratory, Los Alamos, NM 87545, USA. (rrl@lanl.gov)